

CONSTRAINING THE PROJECTED RADIAL DISTRIBUTION OF GALACTIC SATELLITES WITH THE SLOAN DIGITAL SKY SURVEY

JACQUELINE CHEN¹, ANDREY V. KRAVTSOV^{1,2}, FRANCISCO PRADA³, ERIN S. SHELDON⁴, ANATOLY A. KLYPIN⁵,
MICHAEL R. BLANTON⁴, JONATHAN BRINKMANN⁶, & ANIRUDDHA R. THAKAR⁷

Draft version June 27, 2018

ABSTRACT

We use the Sloan Digital Sky Survey (SDSS) spectroscopic sample to constrain the projected radial distribution of satellites around isolated $\sim L_*$ galaxies. We employ mock galaxy catalogs derived from high-resolution cosmological simulations to investigate the effects of interloper contamination and show that interlopers significantly bias the estimated slope of the projected radial distribution of satellites. We also show that the distribution of interlopers around galaxies is expected to be non-uniform in velocity space because galaxies are clustered and reside in crowded environments. Successful methods of interloper contamination correction should therefore take into account environments of the host galaxies. Two such new methods are presented and the most reliable of them is used to correct for interloper contamination in analyses of the SDSS galaxy sample. The best fit power-law slope of the interloper-corrected surface density distribution of satellites, $\Sigma(R) \propto R^\alpha$, in the volume-limited SDSS sample is $\alpha \simeq -1.7 \pm 0.1$, independent of the galaxy and satellite luminosities. Comparison with Λ CDM simulations shows that the radial distribution of the SDSS satellites is more concentrated than that of subhalos around galaxy-sized halos, especially at $R < 100h^{-1}$ kpc. The predicted dark matter radial distribution is somewhat more concentrated than the profile of the SDSS satellites, but the difference is not statistically significant for our sample.

Subject headings: cosmology: theory – dark matter – galaxies: formation – galaxies: structure – galaxies: fundamental parameters

1. INTRODUCTION

In the Cold Dark Matter (CDM) paradigm, satellite galaxies are expected to be associated with the dark matter subhalos – halos which lie within the virial radius of a larger halo – ubiquitous in the cosmological CDM simulations. The abundance and radial distribution of satellite galaxies can therefore serve as a useful test of CDM galaxy formation models, constraining the relation between galaxies and subhalos. In addition, satellite dynamics can provide useful constraints on the total mass distribution in galactic halos (e.g., Zaritsky & White 1994; Zaritsky et al. 1997; Prada et al. 2003; van den Bosch et al. 2004; Conroy et al. 2005a). This, however, requires a good understanding of how the spatial distribution and kinematics of satellites and dark matter are related.

Many recent studies based on numerical simulations have shown that the radial distribution of subhalos in cluster-sized systems is less concentrated than that

of dark matter in the inner $\approx 20 - 50\%$ of the virial radius of host halos, but approximately follows the dark matter distribution at larger radii (Ghigna et al. 1998; Colin et al. 1999; Ghigna et al. 2000; Springel et al. 2001; De Lucia et al. 2004; Diemand et al. 2004; Gao et al. 2004; Nagai & Kravtsov 2005). Theoretical predictions for galaxy distributions in clusters have also been accompanied by rapidly improving observational measurements (e.g., Lin et al. 2004; Hansen et al. 2005; Collister & Lahav 2005; Yang et al. 2005; Coil et al. 2006), which also find concentrations of galaxy radial profiles lower than the concentrations expected for the matter distribution of their parent halos.

The observed distribution of satellite galaxies in galactic halos has been studied less extensively. The Local Group dwarf population is more radially concentrated than subhalos in dissipationless numerical simulations (Kravtsov et al. 2004b; Taylor et al. 2004; Willman et al. 2004), a bias that is likely related to the physics of the formation of the smallest dwarf galaxies (Kravtsov et al. 2004b; Diemand et al. 2005). The known population of the Local Group satellites is, however, quite small compared to the expected population of CDM subhalos (Klypin et al. 1999b; Moore et al. 1999). Moreover, the strong radial bias exhibited by the faint Milky Way satellites is not expected to apply to the brighter satellites (such as, for example, the Magellanic Clouds).

More accurate, statistical constraints on the satellite distribution can be obtained by using galaxy redshift surveys. Several early studies attempted to constrain the small-scale galaxy correlation function by estimating the surface density of objects projected near galaxies, $\Sigma(R) \propto R^\alpha$, finding slopes

¹ Dept. of Astronomy and Astrophysics, Kavli Institute for Cosmological Physics, The University of Chicago, Chicago, IL 60637; jchen.andrey@oddjob.uchicago.edu

² Enrico Fermi Institute, The University of Chicago, Chicago, IL 60637

³ Ramón y Cajal Fellow, Instituto de Astrofísica de Andalucía (CSIC), E-18008 Granada, Spain; fprada@iaa.es

⁴ Center for Cosmology & Particle Physics, Dept. of Physics, New York University, 4 Washington Place, New York, NY 10003; erin.sheldon,michael.blanton@gmail.com

⁵ Astronomy Dept., New Mexico State University, MSC 4500, P.O. Box 30001, Las Cruces, NM 88003-8001; aklypin@nmsu.edu

⁶ Apache Point Observatory, P.O. Box 59, Sunspot, NM 88349; jb@apo.nmsu.edu

⁷ Department of Physics & Astronomy, The Johns Hopkins University, 3400 North Charles Street, Baltimore, MD 21218; thakar@jhu.edu

ranging from $\alpha = -0.5$ to -1.25 (Lake & Tremaine 1980; Phillipps & Shanks 1987; Vader & Sandage 1991; Lorrimer et al. 1994; Smith et al. 2004; Madore et al. 2004).

Recently, the availability of large galaxy redshift surveys has allowed construction of large statistical samples of parent galaxies and satellites with well defined selection criteria. The large sample sizes and redshift information make it possible to understand the biases and completeness of the sample. In addition, isolation criteria for the primaries can be introduced in order to reduce the interloper contamination and simplify the interpretation of results. van den Bosch et al. (2005) use mock galaxy redshift samples derived from large cosmological simulations to develop an iterative method of interloper rejection for the Two Degree Field Galaxy Redshift Survey (2dFGRS) and find that the data is generally consistent with the dark matter profile at large projected radii, but conclude that incompleteness of close pairs in the survey prevent strong constraints. In an independent analysis, Sales & Lambas (2005) account for the close-pair bias in the data by estimating completeness with control samples of objects that are not physically bound to the primaries. They estimate the power-law slope of the satellite distribution to be $\alpha = -0.96 \pm 0.03$ for projected radii between 20 and $500 h^{-1}$ kpc with a significant dependence on morphological type of the parent galaxies ($\alpha \approx -1.1$ for the early type, and ≈ -0.7 for the late type galaxies). Note, however, that these values of α are obtained without any correction for interlopers.

Given that the satellite distribution can be directly probed only in projection, with only limited information about positions of likely satellites in three dimensions, one has to worry about contamination by interlopers, the objects that are not true satellites but are simply close to the parent due to projection. Unfortunately, in practice it is often tricky to estimate and correct for the interloper contamination. This is especially difficult if the redshift information is absent as was the case in the earliest studies of the satellite distribution. However, even in studies in which redshift information is available, the interlopers are often neglected (e.g., Sales & Lambas 2005). Nevertheless, as we show in this paper, the effect of interlopers must be corrected for in order to obtain an unbiased measurement of the satellite projected radial distribution.

The simplest assumption one can make is that the surface density of interlopers is uniform. The interloper contamination can then be estimated by sampling the environments around random points in the field. This method thus presumes that the volume around a random point on the sky and in redshift space contains a representative density of interlopers. However, bright galaxies are strongly correlated in space and thus can be expected to be preferentially located in crowded environments. One may suspect, then, that the random points method can underestimate the interloper number density around real galaxies. Therefore, more sophisticated methods, which sample interlopers in the environments similar to those of the primary galaxies, need to be developed.

In this study, we develop two new methods to estimate the contribution of interlopers to the surface density of satellites, which take into account the clustering of par-

ent galaxies. We use cosmological simulations to test different methods of interloper subtraction and present detailed discussion of their strengths and weaknesses. We show that interloper contamination can significantly bias measurements of the projected radial distribution of satellite galaxies. Proper interloper subtraction is, therefore, a must in studies of the radial distribution of satellites. We use the Sloan Digital Sky Survey (SDSS) spectroscopic sample to measure the projected radial distribution of satellites around nearby bright galaxies, corrected for interlopers. We compare the result to the predictions for the dark matter and subhalo distribution in the Λ CDM cosmology.

The paper is organized as follows. In § 2 we discuss the interloper contamination and different methods of interloper subtraction, testing each of them using mock satellite catalogs derived from cosmological simulations. We then describe our SDSS spectroscopic galaxy sample and the selection of primaries and satellites in § 3. In § 4 we derive the interloper-corrected surface density profile of satellites in volume-limited and flux-limited SDSS samples, and their subsamples, and compare results to the Λ CDM cosmological simulations. We also discuss comparisons to simulations results. Our main results and conclusions are summarized in section §5. Throughout this paper, we assume flat Λ CDM cosmology with $\Omega_m = 0.3$ and $h = 0.7$.

2. INTERLOPER SUBTRACTION

We use cosmological N -body simulations to construct mock samples of host halos and possible satellites, with which we can examine the effects of interloper contamination on the satellite distributions and test different methods of interloper subtraction. We start with two $80h^{-1}$ Mpc high-resolution dark matter simulations of the concordance Λ CDM cosmology: $\Omega_m=0.3$, $h=0.7$, and $\sigma_8=0.9$. The two simulations differ in the random seed of their initial conditions. We use outputs of the simulations at a redshift of 0.1, which is similar to the average redshift of objects in the SDSS spectroscopic survey. The simulations were performed with the Adaptive Refinement Tree (ART) N -body code (Kravtsov et al. 1997; Kravtsov 1999). Details of the simulations can be found in Tasitsiomi et al. (2004). Halo identification was performed using a variant of the Bound Density maxima halo finding algorithm (Klypin et al. 1999a). Details of the algorithm and parameters used in the halo finder can be found in Kravtsov et al. (2004a).

In addition, we use a simple, observationally motivated scheme to assign luminosities to the halos. Details of this method can be found in Tasitsiomi et al. (2004). Halos are assigned luminosities by matching the cumulative velocity function, $n(> V_{\max})$, where V_{\max} is the maximum circular velocity, to the SDSS luminosity function, $n(< M_r)$ at $z = 0.1$ (Blanton et al. 2003c). M_r is the SDSS r -band absolute magnitude defined as $M - 5\log h$. The magnitudes have been K-corrected to $z=0.0$, using `kcorrect v3.2` (Blanton et al. 2003c). Scatter is introduced in the relation between V_{\max} and M_r , assuming a standard deviation of 1.5 magnitudes for the M_r distribution at fixed V_{\max} . All galaxies down to $M_r = -18$ (corresponding to a mean minimum $V_{\max} = 100 \text{ km s}^{-1}$) are included.

In the remainder of the paper, our terminology is to re-

TABLE 1
SELECTION & ISOLATION CRITERIA FOR TEST SAMPLES

Parameters	Test Sample 1 (TS1)	Test Sample 2 (TS2)	Test Sample 3 (TS3)
Constraints on primaries	$V_{\max} = 100\text{-}150, \dots, 300\text{-}350 \text{ km s}^{-1}$	$M_r < -20$	$M_r < -20$
Satellite objects	DM particles	DM particles	satellite galaxies
Isolation criteria:			
Size difference	$V_{\max} > 0.5V_{\max}^{\text{pri}}$	$V_{\max} > 0.5V_{\max}^{\text{pri}}$	$\Delta M_r < 2$
Minimum projected distance, $\Delta R (h^{-1} \text{ Mpc})$	0.5	0.5	0.5
Minimum velocity separation, $\Delta V (\text{km s}^{-1})$	1000	1000	1000
Satellite sample criteria:			
Magnitude difference from the primary	—	—	$\Delta M_r > 2$
Maximum projected distance, $\delta r (h^{-1} \text{ Mpc})$	0.6	0.6	0.6
Maximum velocity separation, $\delta v (\text{km s}^{-1})$	500	500	500, 1000
Number of isolated primaries	380, 289, 236, 143, 89	728	728
Number in satellite sample	7475, 11165, 16614, 15354, 14899	50608	343, 401
Limiting magnitude M_r	—	—	-18

fer to the sample of hosts or primaries constructed using isolated DM halos (i.e., objects which do not lie within a virial radius of a larger object) selected by their maximum circular velocities as a sample of “halos” and the sample of isolated DM halos assigned r -band luminosities as a sample of “galaxies,” respectively. We use V_{\max} to quantify the size of halos because it is measured more robustly and not subject to the same ambiguity as mass definitions. For “galaxies”, we use magnitudes, M_r , to quantify the size of galaxies, as an alternative to V_{\max} to account for possible effects of scatter between V_{\max} and M_r .

For possible satellites, subhalos assigned r -band luminosities are referred to as ‘satellite galaxies’ and are selected by their M_r magnitude difference from their parent ‘galaxies.’ For isolated halos, satellites are selected from an arbitrary fraction of dark matter particles around each host halo. These two choices of test satellite samples are expected to bracket the possible range of radial profiles of the real satellites (Diemand et al. 2004; Nagai & Kravtsov 2005). Below we detail the definition of samples in our analysis.

2.1. Primary and Satellite Samples

Previous studies of the projected distribution of galactic satellites used observationally motivated selection criteria to construct a primary sample of isolated host galaxies and a sample of potential satellites that are projected close to primaries. To test several alternative methods for interloper subtraction, we construct a set of primary and satellite samples derived from simulations using different isolation criteria for the primaries and different selection of the satellite samples.

For the primaries we use isolation criteria similar to those of Prada et al. (2003). We start by creating primary samples of halos and galaxies. An isolated primary halo, with circular velocity V_{\max}^{pri} , must have no other halos with a maximum circular velocity $V_{\max} > 0.5 V_{\max}^{\text{pri}}$ (which corresponds to an absolute magnitude difference of $\approx 1.5 - 2$ magnitudes) within a projected separa-

tion $\Delta R = 0.5h^{-1} \text{ Mpc}$ and velocity separation, $\Delta V = 1000 \text{ km s}^{-1}$. An isolated galaxy primary with absolute magnitude M_r^{pri} must have no other galaxies brighter than $M_r^{\text{pri}} + 2$, within the same projected separation and velocity separation.

For each isolated primary, we construct two satellite samples. In the first, we use a random subset of DM particles found within a projected distance, $\delta r = 0.6 h^{-1} \text{ Mpc}$, and velocity difference, $\Delta v = 500 \text{ km s}^{-1}$, from each primary. These are our fiducial choices of δr and δv . We also test a non-fiducial velocity difference, $\delta v = 1000 \text{ km s}^{-1}$. In the second satellite sample, we select all galaxies fainter than the primary by more than two magnitudes, within the same projected distances and velocity difference as above.

For our primary halos, we create several DM particle satellite samples for different ranges of V_{\max}^{pri} (100-150, 150-200, 200-250, 250-300, 300-350 km s^{-1}). This set of DM halo primaries and DM particle satellites is referred to hereafter as Test Sample 1. For primary galaxies, we use a single sample of 728 galaxies with $M_r < -20$ and build three different satellite samples using DM particles with the $\delta v = 500 \text{ km s}^{-1}$ criterion, satellite galaxies with $\delta v = 500 \text{ km s}^{-1}$, and satellite galaxies with $\delta v = 1000 \text{ km s}^{-1}$. The set of primary galaxies and DM particle satellites is referred to as Test Sample 2, while the set using satellite galaxies – subhalos with assigned luminosities – and both velocity criteria is labeled Test Sample 3. These samples are summarized in Table 1. For samples with DM satellite particles, we bin the objects in radial bins of $35h^{-1} \text{ kpc}$, starting at a minimum separation of $25.6h^{-1} \text{ kpc}$. For samples with satellite galaxies, we bin objects in bins of $70h^{-1} \text{ kpc}$, starting at the same minimum separation. The larger bin in the latter case is due to the smaller statistics of the subhalo satellite sample.

2.2. True Satellites vs. Interlopers

There is a fraction of objects in our satellite samples that are not gravitationally bound to the primaries but are included in the sample because of projection effects.

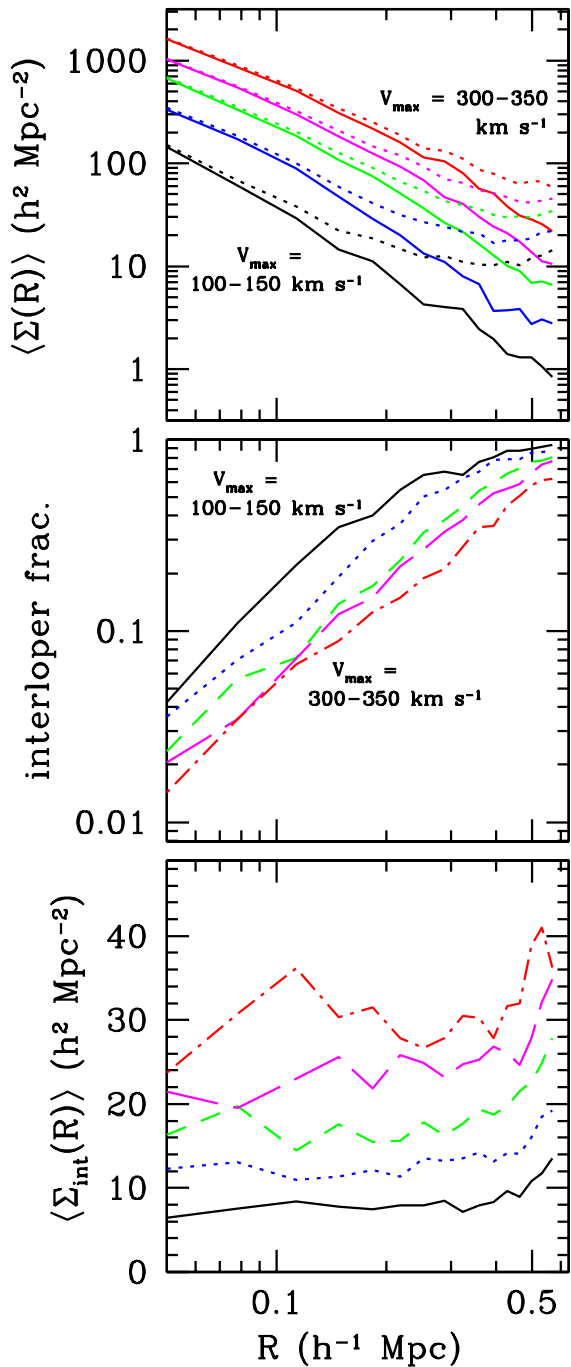


FIG. 1.— Testing interloper subtraction with mock catalogs: the derived average projected distribution of satellites compared to true satellites for the mock samples with five $V_{\text{max}}^{\text{pri}}$ ranges: 100-150, 150-200, 200-250, 250-300, and 300-350 km s^{-1} (Test Sample 1). *Top*: The projected radial number density profile for true satellites (solid) and the satellite sample (dotted). The amplitude in number density increases with $V_{\text{max}}^{\text{pri}}$. *Center*: The fraction of interlopers in the satellite sample as a function of projected radius. The bins are distinguished by line type: 100-150 (solid), 150-200 (dotted), 200-250 (short dashes), 250-300 (long dashes), and 300-350 (dot-dashed) km s^{-1} . *Bottom*: The projected interloper number density profile using the same line types as the center panel.

Throughout this paper, we call such objects *interlopers*. We define true satellites as objects which satisfy the following negative binding energy criterion:

$$E < \frac{1}{2}|V|^2 + \phi(r), \text{ where } \phi(r) = -\frac{v_{\text{esc}}^2(r)}{2}. \quad (1)$$

Here $\mathbf{V} = \mathbf{v}_{\text{sat}} - \mathbf{v}_{\text{pri}}$ is the 3D satellite velocity with respect to the primary, and, for a Navarro et al. (1997, hereafter NFW) profile,

$$v_{\text{esc}}^2(r) = 9.26 V_{\text{max}}^2 \frac{\ln(1+r/r_s)}{r/r_s}, \quad (2)$$

where r_s has been estimated as $r_s = r_{\text{max}}/2.15$ and r_{max} is the radius of the maximum circular velocity of the host halo, V_{max} , as expected for a NFW density profile.

Using our test samples, we look for biases in the true satellite surface density profile and the projected distribution of the satellite sample. We calculate the surface density of satellites per primary by

$$\langle \Sigma(R) \rangle = \frac{N_{\text{bin}}}{\pi N_{\text{pri}}(R_2^2 - R_1^2)}, \quad (3)$$

where N_{bin} is the number of objects in the satellite sample that are found between the inner, R_1 and outer, R_2 , radii of the annulus and N_{pri} is the number of objects in the primary sample. R is the midpoint of the bin.

The projected number density profiles of all satellites and only true satellites as a function of distance to the primary for Test Sample 1 are plotted in the top panel of Figure 1. Here we can see that interlopers significantly flatten the projected radial distribution. The flattening is the strongest for the surface density profiles of satellite samples of the smallest primary halos. For the different $V_{\text{max}}^{\text{pri}}$ primary samples, the DM particle satellite samples show that the fraction of interlopers in the satellite sample as a function of projected radius is similar for all mass ranges, but decreases with increasing primary mass. In addition, at all masses, the projected number density of interlopers (bottom panel of Fig. 1) is relatively flat, but rises at radii greater than the isolation criterion. The results for Test Samples 2 and 3 are similar to those shown in Figure 1.

2.3. Interloper Subtraction Methods

2.3.1. Random Points Method

The most straightforward procedure for interloper removal, which we call the random points method, assumes that the surface density of interlopers is constant and can be estimated by surveying the area around randomly placed points (e.g., Lake & Tremaine 1980). This is one of the simplest methods to apply, since it can be implemented even without redshift information.

We apply this method to our simulation-derived samples, by choosing random points within the simulation box which satisfy the same isolation criteria as the corresponding primary sample. Each of these random points, which make up a mock primary sample, has the characteristics – mass, magnitude, and velocity – of an object in the real sample of primaries. This is accomplished by sampling the primary sample with replacement – i.e., assigning each random point with the characteristics of an object in the primary sample, choosing that object randomly from the entire primary sample. To estimate the

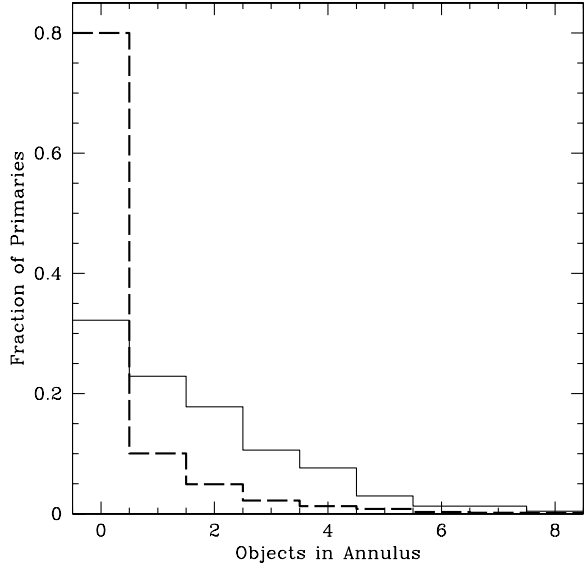


FIG. 2.— The fraction of primaries with a number of objects with $V_{\max} > 0.5V_{\max}^{\text{pri}}$ in the annulus of $0.5 < \Delta R < 1.0h^{-1}$ Mpc and $\Delta V \leq 500 \text{ km s}^{-1}$. The primary sample of $V_{\max} = 200\text{-}250 \text{ km s}^{-1}$ (Test Sample 1) is plotted here (thin, solid line) and the corresponding random points mock primary sample is shown in the thick, dashed line.

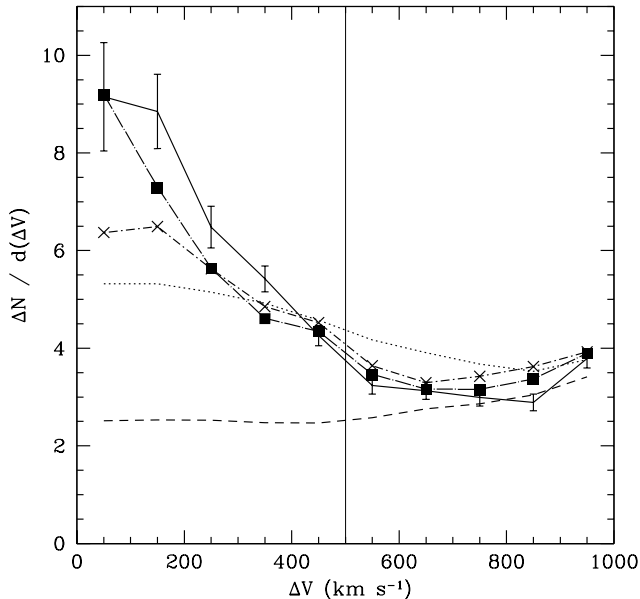


FIG. 3.— Testing interloper substructure with mock catalogs: the relative velocity distribution of the interloper sample in the mock catalog for primaries with $V_{\max} = 200 - 250 \text{ km s}^{-1}$ (Test Sample 1) for all DM particles within $25.6 < \Delta R < 500h^{-1}$ kpc (solid line, Poisson errors). The estimated interloper sample for the clustered random points method is shown as a dotted line and for the random points method as a dashed line. The nearby points methods are shown in dot-dashed lines, with square points for $\Delta R_{\text{corr}} = 1 - 2h^{-1}$ Mpc and crosses for $\Delta R_{\text{corr}} = 1 - 5h^{-1}$ Mpc. The thin vertical line shows the velocity difference criterion of the satellite sample of 500 km s^{-1} .

points that has 20 times the number of objects in the sample of primaries. We can expect, however, that uniformly distributed random points will preferentially sample voids rather than the environments similar to those of the isolated primaries. This is because 1) voids occupy most of the volume and 2) our isolation criteria have forced the random points to preferentially lie in voids, because the fraction of space that satisfies our isolation criteria is larger in voids than in dense environments.

This is illustrated in Figure 2, which shows the distribution of massive ($V_{\max} > 0.5V_{\max}^{\text{pri}}$) neighbors within the annulus described by the projected separation of $0.5 < \Delta R < 1.0h^{-1}$ Mpc (i.e., just outside the radius used in the isolation criteria) and velocity difference of $\Delta V = 500 \text{ km s}^{-1}$ for our sample of primaries (Test Sample 1) and the sample of random points satisfying the same isolation criteria. The Figure 2 shows that primaries have systematically larger number of massive neighbors than the random points, and, therefore, that primaries occupy clustered regions of space. The random points method is thus expected to consistently underestimate the interloper contamination. This result may also be surmised from the bottom panel of Fig. 1, which shows that the number density of interlopers is not uniform and is correlated with primary halo mass. More massive isolated halos have more interlopers, which is consistent with the concept that, in general, more massive objects are more clustered.

2.3.2. Clustered Random Points Method

It is clear that we can improve upon the random points method, if we select not random points but points that are in environments similar to those of primary galaxies. We attempt to achieve this in the clustered random points method. Isolated points are chosen at random and the number of objects in the annulus described above is calculated. Points that allow the fractional distribution of annular objects from the clustered random points to exceed that of the primary points are rejected. In other words, the method insures that the mock sample contains the same distribution of massive neighbors around the primaries, as shown in Figure 2. As we discuss below, the clustered random points method performs consistently better than the random points method in estimating the interloper contamination.

In Figure 3, we show the relative velocity distribution of interlopers and estimated interlopers for primaries with $V_{\max} = 200 - 250 \text{ km s}^{-1}$ in Test Sample 1. The interloper distribution is not constant as a function of velocity, showing a peak at $\Delta V = 0$ and a tail to $\Delta V = 1000 \text{ km s}^{-1}$. The interloper population includes not just objects uniformly distributed in the velocity space, but also objects with velocities correlated with the velocity of the primaries. The estimated interloper population using the random points is uniformly distributed in velocity space and significantly underestimates the interloper contribution (dashed line). The clustered random points method fares considerably better, although the number of interlopers is still somewhat underestimated (dotted line).

2.3.3. Nearby Points Method

An alternative way of ensuring that the random points sample environments of the primaries correctly is to pick

interloper contribution, we construct a sample of random

isolated points that are within a projected correlation length of real primaries. Smith et al. (2004) use such a method, estimating the background using points at projected distances $> 350h^{-1}$ kpc. In their isolation criteria, they require that the magnitude difference between a neighbor and the primary must be greater than 0.7 magnitudes for galaxies within a projected distance of $700h^{-1}$ kpc. The area outside of a $350h^{-1}$ kpc projected radius, however, may not have the same isolation criteria as the primary galaxy sample.

Observational measurements of the two-point correlation function of bright galaxies find a correlation length of $\approx 5h^{-1}$ Mpc (e.g., Zehavi et al. 2004). In Figure 3, we show the estimated fraction of interlopers using a method in which test points are selected from the annuli of $\Delta R_{\text{corr}} = 1 - 2h^{-1}$ Mpc and $\Delta R_{\text{corr}} = 1 - 5h^{-1}$ Mpc around the primaries. We choose the inner radius of $1h^{-1}$ Mpc to avoid sampling real satellites. All test points satisfy the same isolation criteria as our sample of primaries. The Figure 3 shows that the velocity distribution of interlopers for $\Delta R_{\text{corr}} = 1 - 5h^{-1}$ Mpc is somewhat similar to that of the clustered random points method, while $\Delta R_{\text{corr}} = 1 - 2h^{-1}$ Mpc choice recovers the true interloper velocity distribution much better. We will, therefore, use this latter radial annulus as our fiducial choice. As we show below, the nearby points method with the fiducial ΔR_{corr} is the best among the other methods we tested here in recovering the interloper contamination in our mock samples.

2.3.4. "Gaussian + Constant" Method

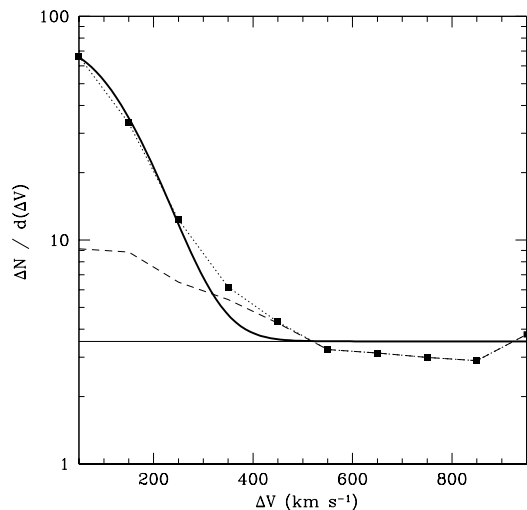


FIG. 4.— The Gaussian plus constant method (thick, solid line) is compared to the velocity distribution of the satellite sample (square points, dotted line) and the interloper sample (dashed line) for primaries with $V_{\text{max}} = 200\text{--}250$ km s $^{-1}$ and satellites with $25.6 < \Delta R < 500h^{-1}$ kpc (Test Sample 1). The thin horizontal line shows the estimated interloper fraction from the Gaussian plus constant method.

For completeness, we also test the interloper subtraction method used by McKay et al. (2002) and Prada et al. (2003). The method does not use random points, but assumes instead that the velocity distribution of satellites can be described by a Gaussian, while

the distribution of interlopers is uniform. The velocity distribution of interlopers shown in Figure 3 is inconsistent with this assumption; a result that is in agreement with conclusions by van den Bosch et al. (2004, see their Fig. 1).

Nevertheless, the tests performed on our mock samples show that the method does estimate the velocity dispersion of the true satellites – the purpose for which the method was originally used by McKay et al. (2002) and Prada et al. (2003) – quite accurately. This is because the velocity dispersion of the interlopers, correlated with primaries in velocity space, is similar to that of the satellites. Their inclusion into the satellite samples thus does not bias the velocity dispersion appreciably. The velocity dispersion of interlopers is likely due to the infall of objects along filaments.

Nevertheless, to correctly account for the interloper contribution to the radial surface density profile this is not sufficient. The assumption that all of the objects correlated with the primary in velocity space are true satellites will lead to an underestimate of interloper contribution. This is demonstrated in Figure 4. Given that the interloper fraction increases with increasing projected radius, the "Gaussian plus constant" method leads to surface density profiles flatter than the true distribution. Another problem occurs when the number of satellites is small and their velocity distribution is not well sampled. We find that in such cases the Gaussian+constant fits can be unstable.

In our tests, we use objects within $\delta v = 1000$ km s $^{-1}$ to fit a gaussian+constant. This is larger than $\delta v = 500$ km s $^{-1}$ used by Prada et al. (2003) and in this paper fiducially, because our sample includes massive objects with velocity dispersion close to the δv , in which case the interloper constant is poorly constrained.

2.4. Testing the Interloper Subtraction Methods

We compare how well the four different interloper subtraction methods described above recover the true projected density profile of satellites $\langle \Sigma(R) \rangle_{\text{true}}$, where

$$\langle \Sigma(R) \rangle_{\text{int sub}} = \langle \Sigma(R) \rangle_{\text{sat}} - \langle \Sigma(R) \rangle_{\text{est int}}, \quad (4)$$

where our interloper subtracted density profile, $\langle \Sigma(R) \rangle_{\text{int sub}}$, is the profile of the satellite sample, $\langle \Sigma(R) \rangle_{\text{sat}}$, minus the interloper profile, $\langle \Sigma(R) \rangle_{\text{est int}}$, estimated using different methods described above.

Figure 5 shows the results for Test Sample 1, for different $V_{\text{max}}^{\text{Pri}}$ ranges of our primaries. The figure shows that the random points method performs the worst. The "Gaussian plus constant" and clustered random points methods perform better, although the latter does a better job overall in estimating the interloper contamination. The nearby points performs best. For Test Sample 2 and 3, the results are similar, except for the "Gaussian plus constant" method, which runs into difficulties with fitting correct interloper level for Test Sample 3, in which the number of satellites is small and the velocity distribution is under-sampled. This indicates that the method should be applied only to the samples in which the velocity distribution of satellites and interlopers is sampled well.

2.5. Fits to the radial profiles

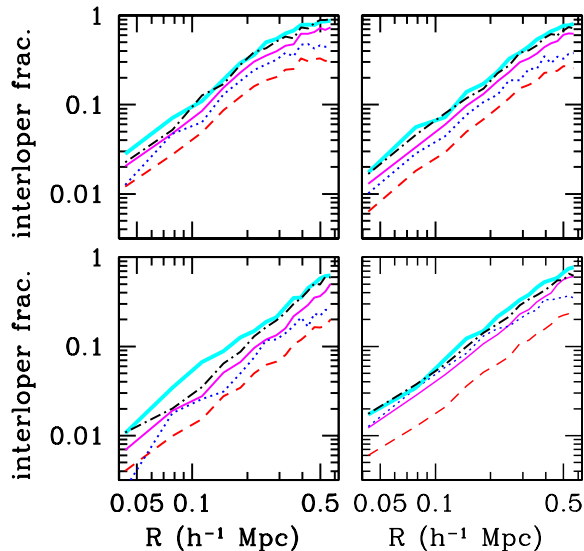


FIG. 5.— Testing interloper subtraction with mock catalogs: the fraction of interlopers for different mock satellite samples estimated by different methods. Clockwise from the top, left panel, the V_{\max} ranges are 150-200, 200-250, 250-300, and 300-350 km s^{-1} , using DM particle satellites (Test Sample 1). The corresponding number density profiles are shown in Fig. 1 (top panel). In all plots, the thick lines represent the true interloper fraction (also shown in Fig. 1, center panel), the dotted lines use the Gaussian plus constant method, the dashed lines use the random points method, the solid lines use the clustered random points method, and the dot-dashed lines use the nearby points method, with $\Delta R_{\text{corr}} = 1 - 2h^{-1}$ Mpc.

We now test how well the fits to the interloper subtracted radial surface density profiles recover the profile of the true satellites. The data is binned with bins of $35h^{-1}$ kpc starting at a projected radius of $25.6h^{-1}$ kpc for the DM particles as satellites, and with bins of $70h^{-1}$ kpc for subhalos with assigned luminosities starting at a projected radius of $25.6h^{-1}$ kpc. We fit the number density profile with a power law,

$$\Sigma(R) = AR^\alpha, \quad (5)$$

for bins with mean projected radius smaller than $0.5h^{-1}$ Mpc. We find the best fit values of the slope, α , and its errors marginalized over the normalization of the power law, for the true satellite sample, the satellite sample (true satellites + interlopers), and for the interloper subtracted profile obtained with each of the methods discussed above. We measure the 1σ errors in slope, which reflects the statistical Poisson errors of the density profiles.

In general, the true DM particle satellite distribution should be well-approximated by a projected NFW profile. However, we do not attempt to fit an NFW profile because, as we can see below, the current observational samples cannot discriminate between the NFW and a simpler power-law profile. We choose our sample of primaries (Test Samples 2 & 3) using luminosities instead of V_{\max} and stack the satellites of many primaries, possibly mixing NFW profiles with different concentrations and virial radii together. In addition, due to the limited satellite statistics and the fiber collisions in the SDSS we use a minimum projected radius, similar to that used in the SDSS spectroscopic sample (see below), which is of

order of 10% of the virial radius of the primary galaxies. The minimum radius, then, may be larger than the scale radius of the NFW profile.

As can be seen from Tables 2 and 3, the DM particle satellite sample (Test Sample 2) and the galaxy satellite sample (Test Sample 3) have different radial distributions. Most of the DM particles in the satellite sample are from the smooth distribution of the parent halo, not subhalos, which explains the steep, $\alpha = -1.81 \pm 0.01$, slope found for the DM particle satellite population. This is consistent with the steep slope of ≈ -3 (or ~ -2 in projection) predicted for the 3-D density profile of the CDM halos at large radii. The radial distribution of the satellite sample which uses subhalos with assigned luminosities is considerably flatter $\alpha = -1.34 \pm 0.12$. At small projected radii, the profile is flattened by tidal disruption of subhalos.

TABLE 2
ESTIMATED POWER-LAW SLOPE FOR SAMPLE WITH DM PARTICLES
(TEST SAMPLE 2)

Input Data	$25.6 < R < 500h^{-1}$ kpc
true satellites	-1.815 ± 0.007
satellite sample	-1.352 ± 0.007
random points	-1.481 ± 0.008
clustered random points	-1.570 ± 0.008
nearby points ($\Delta R_{\text{corr}} = 1 - 2$)	-1.686 ± 0.009
gaussian + constant	-1.533 ± 0.007

TABLE 3
ESTIMATED POWER-LAW SLOPE FOR SAMPLE WITH SATELLITE
GALAXIES (TEST SAMPLE 3)

Input Data	$25.6 < R < 500h^{-1}$ kpc
$\delta v = 500 \text{ km s}^{-1}$	
true satellites	-1.34 ± 0.12
satellite sample	-0.84 ± 0.11
random points	-0.95 ± 0.12
clustered random points	-1.08 ± 0.12
nearby points ($\Delta R_{\text{corr}} = 1 - 2$)	-1.20 ± 0.14
gaussian + constant	-0.95 ± 0.11
$\delta v = 1000 \text{ km s}^{-1}$	
true satellites	-1.34 ± 0.12
satellite sample	-0.75 ± 0.11
random points	-0.95 ± 0.12
clustered random points	-1.23 ± 0.14
nearby points ($\Delta R_{\text{corr}} = 1 - 2$)	-1.24 ± 0.15
gaussian + constant	-0.94 ± 0.11

In Tables 2 and 3, we show that the best-fit slopes for the satellite radial profile are significantly flattened by interlopers. Without any interloper subtraction, the estimated surface density profile will be shallower than the profile of the true satellite population, in both the

DM particle sample and the galaxy sample by ≈ 0.5 in the power-law slope.

The random points method is inadequate for recovering the correct slope: the recovered slope slopes are shallower than those of the true distribution by ≈ 0.4 . The "Gaussian plus constant" method also underestimates the slope significantly. Interloper subtraction by the clustered random points and nearby points perform reasonably well in all test samples. In general, the nearby points method performs the best giving on average a steeper slope (by ≈ 0.1) than the clustered random points method. Overall, the interloper bias still persists as the slope estimated with the nearby points method systematically underestimates the true slope by ≈ 0.1 , even though the slope values estimated with this method are within one standard deviation of the true slope for Test Sample 3. We will therefore use the nearby points method as our interloper correction method of choice, keeping in mind that the best fit slope should be corrected by $\Delta\alpha_{\text{bias}} \approx 0.1$.

3. THE SDSS SPECTROSCOPIC SURVEY

The Sloan Digital Sky Survey (SDSS) (York et al. 2000) will image up to 10^4 deg^2 of the northern Galactic cap in five bands, u, g, r, i, z , down to $r \sim 22.5$ (Fukugita et al. 1996; Hogg et al. 2001; Smith et al. 2002) using a dedicated 2.5m telescope at Apache Point Observatory in New Mexico (Gunn et al. 1998, 2006). In addition to the imaging survey, the SDSS main galaxy sample is a subsample of objects from the imaging catalog which have been targeted for spectroscopic observations (Strauss et al. 2002). The spectroscopic targets are selected with r -band Petrosian magnitudes $r \leq 17.77$ and r -band Petrosian half-light surface brightnesses $\mu_{50} \leq 24.5 \text{ mag arcsec}^{-2}$. The median redshift of the SDSS main galaxy sample is 0.104.

The SDSS spectroscopy is carried out using 640 optical fibers positioned in pre-drilled holes on a circular plate in the focal plane of 3 degrees diameter, with minimum separation between fibers of $55''$. Targeted imaging regions are assigned spectroscopic plates by an adaptive tiling algorithm (Blanton et al. 2003b), which also assigns each object a fiber. An automated pipeline measures the redshifts and classifies the reduced spectra (Stoughton et al. 2002; Pier et al. 2003; Ivezić et al. 2004, D. J. Schlegel et al. 2005, in preparation).

For this catalog we use the reductions of the SDSS spectroscopic data performed by D. J. Schlegel et al. (2005, in preparation) using their reduction code, which extracts the spectra and finds the redshifts. The redshifts found are, over 99% of the time for Main galaxy sample targets, identical to the redshifts found by an alternative pipeline used for the SDSS Archive Servers (M. SubbaRao et al. 2005, in preparation).

For this analysis, we use a subset of the available spectroscopic main galaxy sample released as of Data Release Four (Adelman-McCarthy et al. 2006), but including all of the galaxy sample released as of Data Release Three (Abazajian et al. 2005). This catalog, known as LSS SAMPLE14, is built from the New York University Value-Added Galaxy Catalog (Blanton et al. 2005) and contains 312,777 galaxies. Because the SDSS spectroscopy is taken through circular plates with a finite number of fibers of finite angular size, the spectroscopic

completeness varies across the survey area. The resulting spectroscopic mask is represented by a combination of disks and spherical polygons (Tegmark et al. 2004). Each polygon also contains the completeness, a number between 0 and 1 based on the fraction of targeted galaxies in that region which were observed. We apply this mask to the spectroscopy and include only galaxies from regions where the completeness is greater than 90%, an area of 3448 square degrees. The same criterion is applied for catalogs of clustered random points and nearby points used for the interloper subtraction.

4. RADIAL DISTRIBUTION OF SATELLITES AROUND SDSS PRIMARIES

Unlike the numerical simulations where we have good resolution and 100% completeness, when using spectroscopic data to stack objects and estimate a surface density, we suffer from two major problems: fiber collisions and incompleteness.

As described previously, the minimum separation between fibers, the fiber collision separation, is $55''$. At a redshift of $z = 0.035$, the approximate median of our SDSS sample of primary galaxies, the fiber collision separation is $26.8 h^{-1} \text{ kpc}$. Fiber collisions could bias the small projected radii end of the radial distribution, removing objects that should be counted and tilting it shallower. However, some of the area of the survey has been re-observed and the overlap region could have objects observed with separations as small as the fiber diameter, $3''$. In our samples, we do not use objects at projected radii smaller than the fiber collision separation.

We use the r -band magnitudes in the LSS SAMPLE14 subsample of the SDSS spectroscopic survey, normalized to $h=1$, such that $M_r = M_{0.1r} - 5\log_{10}h$, where $M_{0.1r}$ is the absolute magnitude K -corrected to $z=0.1$ as described in Blanton et al. (2003a). The LSS SAMPLE14 also provides measures of the fraction of objects with spectra in the area of an object. While fiber collisions remove objects from our survey, incompleteness removes area from our survey, which would likely tilt the number density steeper, since there is more area further away from a primary galaxy. Constraining our sample to include only galaxies with a minimum completeness fraction of 90% should lead us to be complete to that level. However, since we need to search the area around each primary galaxy, it is possible that the search area will not be contained on an area of one completeness level but can overlap with an area of a lower completeness percentage. A simple check of this is to calculate an analogue to the projected cross-correlation function, $w(R)$, which is unbiased by incompleteness and can be compared to the projected number density estimated using the random points method. We apply such test and show that incompleteness does not bias our estimates of the radial profiles (see § 4.2).

We create both a volume-limited sample (§ 4.1) and a flux-limited sample (§ 4.3). The flux-limited sample offers better statistics, but it is also biased to brighter satellite objects and the radial profile of satellite galaxies has not been established to be independent of the magnitude of satellites. For this reason, we also test a volume-limited sample with poorer statistics.

4.1. Volume-limited samples

TABLE 4
SELECTION & ISOLATION CRITERIA FOR SDSS SAMPLES

Parameters	Volume-Limited	Flux-Limited
Maximum depth of sample (km s^{-1}).....	13,500	13,500
Constraints on primaries.....	$-23 < M_r < -20$	$-23 < M_r < -20$
Constraints on bright neighbors:		
Maximum magnitude difference.....	2	2
Minimum projected distance, $\Delta R (h^{-1} \text{ Mpc})$	0.5	0.5
Minimum velocity separation, $\Delta V (\text{km s}^{-1})$	1000	1000
Constraints on satellites:		
Minimum magnitude difference.....	2	2
Maximum projected distance, $\delta r (h^{-1} \text{ Mpc})$	0.5	0.5
Maximum velocity separation, $\delta v (\text{km s}^{-1})$	500, 1000	500, 1000
Minimum projected distance, $\delta r (h^{-1} \text{ Mpc})$	0.329, 0.341	0.329, 0.341
Number of isolated primaries.....	871	871
Number in satellite sample.....	336, 357	678, 786
Limiting magnitude M_r	-17.77, -17.85	—

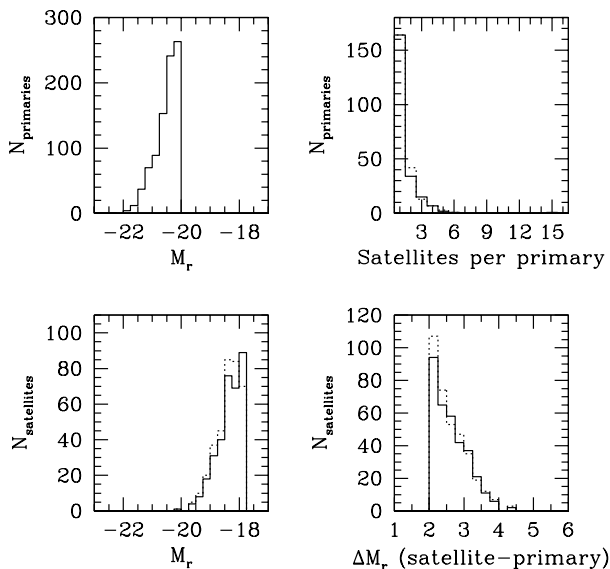


FIG. 6.— Statistics of primaries and satellites for a volume-limited sample. *Top-left*: The r -band magnitude histogram for primaries. *Bottom-left*: The r -band magnitude histogram for satellites. The solid line shows the results for the $\delta v = 500 \text{ km s}^{-1}$ criterion, while the dotted line shows the $\delta v = 1000 \text{ km s}^{-1}$ criterion. *Bottom-right*: The magnitude differences between satellites and primaries, with line styles as in the bottom-left panel. *Top-right*: The number of satellites per primary for primaries with at least one satellite, with line styles as in the bottom-left panel.

We first create a volume-limited galaxy sample from the LSS SAMPLE14 with a depth of $13,500 \text{ km s}^{-1}$, corresponding to the limiting redshift of $z = 0.045$. This limit is chosen as a trade-off between the volume of the sample and the absolute magnitude limit for our satellites, which would need to be decreased to brighter magnitudes for more distant primaries. The trade-off is also with the minimum separation at which fiber-collisions become important, which increases with distance. To include more distant primaries we would have to sacrifice

the ability to probe density distributions at small separations.

In total we have 21,851 galaxies. Since the isolation criterion requires that we search for objects that are within $\Delta V = 1000 \text{ km s}^{-1}$, we can only search for primaries within the subset of velocities 1000 to $12,500 \text{ km s}^{-1}$. For the satellite catalog to be volume-limited, this requires a maximum absolute magnitude of $M_{r,\text{lim}} - 5 \log h = 17.77 - DM - K_{0.1}$ in the r -band, where the 17.77 is the flux limit in this band, DM is the distance modulus, and $K_{0.1}$ is the K -correction at $z=0.1$. We use the K -correction at $z = 0.1$ in order to avoid underestimating the limiting absolute magnitude. As in the simulations, we test both the $\delta v = 500 \text{ km s}^{-1}$ satellite criterion and a larger $\delta v = 1000 \text{ km s}^{-1}$. For those limits, the minimum separation between fibers is $32.9 h^{-1} \text{ kpc}$ and $34.1 h^{-1} \text{ kpc}$, respectively and the limiting absolute magnitudes are -17.77 and -17.85. The satellites are thus limited to the brightest satellite galaxies, $\sim 0.1L_*$. We choose galaxies that are in areas that are at least 90% complete and set the size of the mock primary sample to be 20 times the number of primary galaxies.

TABLE 5
ESTIMATED POWER-LAW SLOPES FOR THE VOLUME-LIMITED SAMPLE

Input Data	
$\delta v = 500 \text{ km s}^{-1}$	
satellite sample	-1.21 ± 0.09
clustered random points	-1.46 ± 0.11
nearby points ($\Delta R_{\text{corr}} = 1 - 2$)	-1.58 ± 0.11
$\delta v = 1000 \text{ km s}^{-1}$	
satellite sample	-1.18 ± 0.09
clustered random points	-1.55 ± 0.11
nearby points ($\Delta R_{\text{corr}} = 1 - 2$)	-1.65 ± 0.12

The statistics of primaries and satellites for both samples are shown in Figure 6. The number of possible satellites found in the volume-limited samples is small. For the range $-23 < M_r < -20$, there are 871 primary galax-

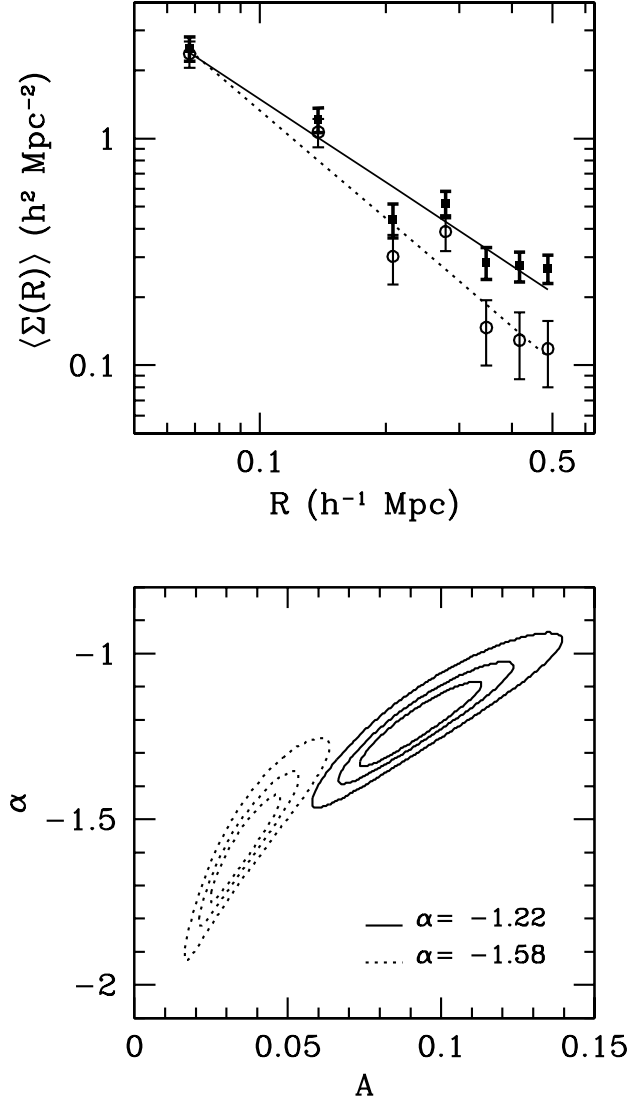


FIG. 7.— The satellite sample compared to interloper subtracted samples for the volume-limited sample using $\delta v = 500 \text{ km s}^{-1}$. *Top*: The best-fit power-law for the satellite sample (solid) and the interloper subtracted profile for the $\Delta R_{\text{corr}} = 1 - 2 h^{-1} \text{ Mpc}$ nearby points (dotted). The data is shown with error bars: satellite sample (square points, thick Poisson error bars) and nearby points (open circles, thin error bars). *Bottom*: The 68%, 90%, and 99% confidence intervals for the satellite sample (solid lines) and the $\Delta R_{\text{corr}} = 1 - 2 h^{-1} \text{ Mpc}$ nearby points sample (dotted lines). The contours are labeled by the unmarginalized best-fit slope of each profile.

ies and 336 objects in the satellite sample with projected radii greater than the minimum separation and less than $0.5 h^{-1} \text{ Mpc}$. For the $\delta v = 1000 \text{ km s}^{-1}$ sample, which uses a slightly larger minimum separation and limiting magnitude, there are 357 galaxies. The volume-limited samples are summarized in Table 4.

The satellite sample and the nearby points interloper subtracted results are shown in Figure 7 for the velocity criterion of $\delta v = 500 \text{ km s}^{-1}$, in bins of $70 h^{-1} \text{ kpc}$, starting from the minimum separation of $32.9 h^{-1} \text{ kpc}$. The results are similar to those in the simulations; the satellite sample distribution is shallower than the inter-

loper subtracted samples. In addition, the nearby points method distribution is steeper than that of the clustered random points method.

We fit the radial profile with a power law, with the results for the slope marginalized over the amplitude of the power law shown in Table 5. The slope of the best-fit power law for the satellite sample is -1.21 ± 0.09 in the sample with $\delta v = 500 \text{ km s}^{-1}$, with very similar results for the $\delta v = 1000 \text{ km s}^{-1}$ sample. The clustered random points method finds a slope of -1.46 ± 0.11 and the nearby points methods finds a slope of -1.58 ± 0.11 in the $\delta v = 500 \text{ km s}^{-1}$ sample. The $\delta v = 1000 \text{ km s}^{-1}$ sample shows steeper fits, with slopes of -1.55 ± 0.11 and 1.65 ± 0.12 , respectively. The systematic differences between the best-fit slopes of the clustered random points and nearby points is ~ 0.1 , consistent with the result found in the simulations. In the simulations, the bias found in the interloper subtraction methods was ~ 0.1 for the nearby points method and ~ 0.2 for the clustered random points method, which would imply that the slope of the true satellite distribution is $\alpha = \alpha_{\text{est}} - \Delta\alpha_{\text{bias}} \approx -1.7$.

The marginalized errors suggest that slopes of the satellite samples and the interloper subtracted samples are significantly different. We illustrate this point in Fig. 7, where we plot all the points at projected radii smaller than $0.5 h^{-1} \text{ Mpc}$ for the $\delta v = 500 \text{ km s}^{-1}$, satellite sample and the results of the nearby points method. Here the best-fit power-law is plotted in the top panel, where the best-fit slope of the satellite sample is $\alpha = -1.22$ and the best-fit slope of the interloper subtracted sample is $\alpha = -1.58$. The bottom panel shows the confidence regions for the two fits, where the slopes of the two distributions do not overlap within the 99% confidence intervals.

4.2. Completeness test

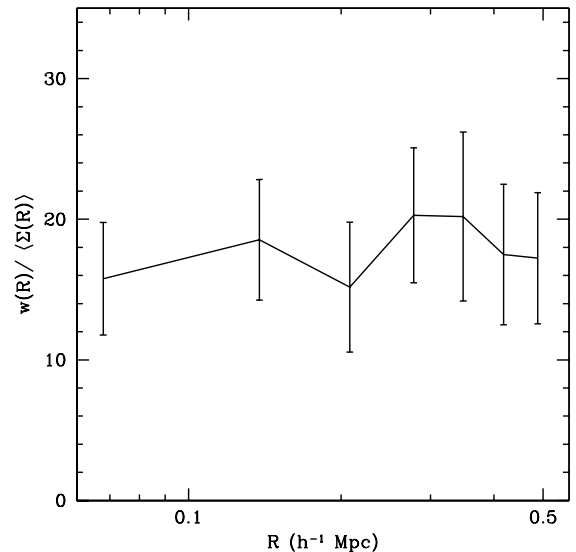


FIG. 8.— The ratio of the cross-correlation function, $w(R)$, to the projected, interloper subtracted surface density of true satellites estimated using the random points method for the volume-limited sample with $\delta v = 500 \text{ km s}^{-1}$.

Although we have selected our sample carefully to

avoid spurious results, we still need to assess to what extent our results might be biased by sample incompleteness, caused by, for example, holes in the survey or edge effects. We can test this by calculating for our primary+ satellite sample a statistic analogous to the projected cross-correlation function:

$$w(R) = \frac{\langle N_{\text{sat}}(R) \rangle}{\langle N_{\text{int}}(R) \rangle} - 1, \quad (6)$$

where $\langle N_{\text{sat}}(R) \rangle = \langle N_{\text{truesat}}(R) \rangle + \langle N_{\text{int}}(R) \rangle$ and $\langle N_{\text{int}}(R) \rangle$ is the estimated number of interlopers at separation R in a sample, and $\langle N_{\text{truesat}}(R) \rangle$ is the corresponding estimated average projected number of the true satellites. For the purposes of this test $\langle N_{\text{int}} \rangle$ is estimated using the random points method (i.e., assuming uniform projected density of interlopers).

The function $w(R)$ can be compared to the surface density of the true satellite galaxies, $\Sigma_{\text{truesat}}(R)$, estimated using the random points method. If the estimate of $\Sigma_{\text{truesat}}(R)$ is affected by incompleteness, the functions $w(R)$ and $\Sigma_{\text{truesat}}(R)$ should have different shapes because $w(R)$ is defined as a ratio of quantities equally affected by area incompleteness, which should cancel out the effect. $\Sigma_{\text{truesat}}(R)$, on the other hand, will be affected. Conversely, $w(R)$ and $\Sigma_{\text{truesat}}(R)$ should have the same shape if effects of incompleteness on $\Sigma_{\text{truesat}}(R)$ are negligible. This is because for the random points interloper subtraction: $\Sigma_{\text{truesat}} = (\langle N_{\text{sat}} \rangle / \langle N_{\text{int}} \rangle - 1) \Sigma_{\text{int}} = w \Sigma_{\text{int}}$, where $\Sigma_{\text{int}}(R) = \text{const}$.

Figure 8 shows the ratio of the surface density profile of satellites estimated for our volume-limited sample using the random points method and function $w(R)$, computed for the same sample. Over the projected radii test, the ratio is consistent with a constant. In addition, the marginalized best-fit slopes of Σ_{truesat} and $w(R)$ agree within statistical errors: $\alpha = -1.33 \pm 0.09$ and $\alpha = -1.41 \pm 0.06$, respectively. We therefore conclude that our measurements of the surface density profiles of satellites are not significantly affected by area incompleteness.

4.3. Flux-limited samples

TABLE 6
ESTIMATED POWER-LAW SLOPES FOR THE FLUX-LIMITED SAMPLE

Input Data	
$\delta v = 500 \text{ km s}^{-1}$	
satellite sample	-1.27 ± 0.06
clustered random points	-1.52 ± 0.07
nearby points ($\Delta R_{\text{corr}} = 1 - 2$)	-1.64 ± 0.07
$\delta v = 1000 \text{ km s}^{-1}$	
satellite sample	-1.17 ± 0.06
clustered random points	-1.56 ± 0.07
nearby points ($\Delta R_{\text{corr}} = 1 - 2$)	-1.66 ± 0.08

We could significantly increase the number of objects in our samples by eliminating the limiting absolute magnitude and increasing the maximum depth of the sample. Increasing the depth, however, will increase the minimum separation of the sample as dictated by the fiber collision problem. We, then, only eliminate the magnitude limit to create a flux-limited sample. For these flux-limited

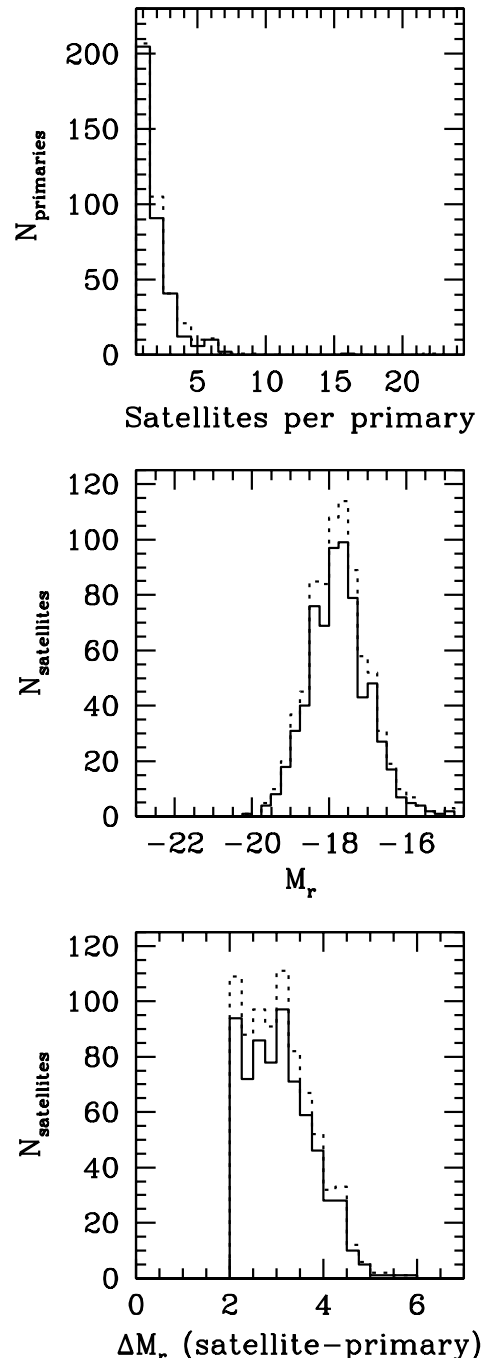


FIG. 9.— Statistics of the satellite samples for a flux-limited sample. The solid line shows the results for the $\delta v = 500 \text{ km s}^{-1}$ criterion, while the dotted line shows the $\delta v = 1000 \text{ km s}^{-1}$ criterion. *Top*: The number of satellites per primary for primaries with at least one satellite. *Center*: The r -band magnitude histogram for satellites. *Bottom*: The magnitude differences between satellites and primaries.

samples, we apply the same isolation and satellite criteria as the volume-limited sample. For the satellite sample with $\delta v = 500 \text{ km s}^{-1}$, we have 678 galaxies. For the larger $\delta v = 1000 \text{ km s}^{-1}$ sample, with a larger minimum separation and limiting magnitude, there are 786 galaxies. The flux-limited samples are summarized in Table

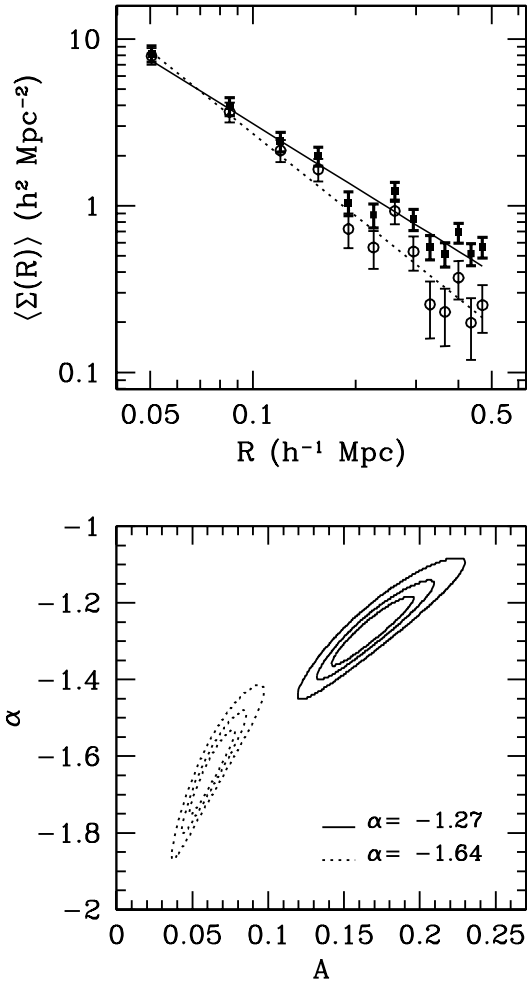


FIG. 10.— The satellite sample compared to interloper subtracted samples for the flux-limited sample with velocity criterion $\delta v = 500 \text{ km s}^{-1}$. *Top*: The best-fit power-law for the satellite sample (solid) and the interloper subtracted profile for the $\Delta R_{\text{corr}} = 1 - 2 h^{-1} \text{ Mpc}$ nearby points (dotted). The data is shown with error bars: satellite sample (square points, thick Poisson error bars) and nearby points (open circles, thin error bars). *Bottom*: The 68%, 90%, and 99% confidence intervals for the satellite sample (solid lines) and the nearby points sample (dotted lines). The contours are labeled by the unmarginalized best-fit slope of each profile.

4. Statistics of the satellite samples in the flux-limited set are plotted in Fig. 9, while the satellite sample and the nearby points interloper subtracted results with $\delta v = 500 \text{ km s}^{-1}$ are plotted in Figure 10 for bins of $35 h^{-1} \text{ kpc}$ starting at the minimum separation of $32.9 h^{-1} \text{ kpc}$. In addition, the marginalized best-fit slopes are listed in Table 6.

The flux-limited results are consistent with those of the volume-limited sample. The clustered random points and nearby points methods for interloper removal once again show steeper profiles than the satellite sample. We also find best-fit power-laws that are similar to the volume-limited sample for the satellite sample ($\alpha = -1.27$) and nearby points method ($\alpha = -1.64$) in the top panel of Fig. 10. The bottom panel shows the confidence regions for the two fits, where the slopes of the two distributions do not overlap within the 99% confidence

intervals.

The marginalized best-fit power-law slope values in Table 6 show similar results to those found in the volume-limited sample. The satellite sample with $\delta v = 500 \text{ km s}^{-1}$ has a somewhat steeper slope than the $\delta v = 1000 \text{ km s}^{-1}$ sample, -1.27 ± 0.06 to -1.17 ± 0.06 . In addition, the clustered random points and nearby points methods produce very consistent results in both samples, $\alpha = -1.52 \pm 0.07$ and $\alpha = -1.64 \pm 0.07$ for the $\delta v = 500 \text{ km s}^{-1}$ sample.

The similarity of the results for the volume-limited and flux-limited samples suggest that the flux-limited data do not induce any bias to the sample while increasing the statistical significance of the results.

4.4. Trends with luminosity

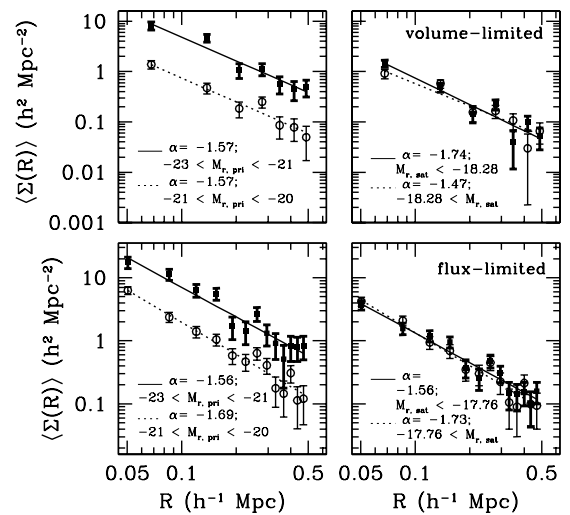


FIG. 11.— The left-hand panels show the results of the nearby points method for samples split by bright and faint primaries. The right-hand panels show the results when samples are split into bright and faint satellites. In all cases, the 'bright' data is shown in square points, with thick error bars and the 'faint' data is shown in open circles with thin error bars. In addition, the unmarginalized best-fit power-law for the 'bright' data is shown with a solid line and a dotted line for the 'faint' data. The top panels show results from the volume-limited sample and the bottom panels show the results from the flux-limited sample.

We now test the projected radial distribution for differences between bright and faint primary galaxies and bright and faint satellites (see Figure 11) for the nearby points method and $\delta v = 500 \text{ km s}^{-1}$. We first split the primary sample into two, a bright sample of $-23 < M_r < -21$ with 125 primaries and a faint sample of $-21 < M_r < -20$ with 746 primaries. The volume-limited set has 161 possible satellites in the bright primaries sample and 171 in the faint primaries sample. The flux-limited set has 225 possible satellites in the bright primaries sample and 297 in the faint primaries sample. The left-hand panels of Figure 11 show that, in all cases, the amplitude of the projected number density profile is always larger for the bright primary samples. The bright and faint primary samples show consistent slopes. The slopes marginalized over the normalization for the bright volume- and flux-limited samples are -1.56 ± 0.14 and -1.55 ± 0.11 , respectively, while the corresponding slopes for the faint samples are -1.57 ± 0.17 and -1.68 ± 0.10 .

We thus do not find a significant dependence of the concentration of the radial profiles on the luminosity of the primary galaxies in the luminosity range probed.

Next, we split the satellite sample into samples of bright and faint satellites at the median absolute magnitude of each satellite sample. The volume-limited set is split at $M_r = -18.28$, while the flux-limited at $M_r = -17.76$. The luminosity range of satellite galaxies probed is not large, with the medians of the satellite samples $\sim 0.1L_*$. The right-hand panels of Fig. 11 show that the best-fit power-law slopes, marginalized over the normalization, for the bright and faint satellites are consistent: -1.72 ± 0.16 and -1.45 ± 0.16 , respectively, for the the volume-limited set, and -1.55 ± 0.11 and 1.72 ± 0.11 for the flux-limited set.

4.5. Putting everything together: comparisons with Λ CDM expectations

In this section we compare the observed projected density profile of satellites in our SDSS sample to mock satellite samples derived from high-resolution simulations of the concordance Λ CDM model. For this comparison, we compare to catalogs that are representative of subhalo, satellite galaxy, and dark matter distributions, interesting reference points to compare to the observational results. In the first catalog, we use samples of isolated halos and subhalos selected simply using their maximum circular velocity, V_{\max} . The only criterion we use for subhalos is $V_{\max} > 100 \text{ km s}^{-1}$ to avoid possible biases due to effects of resolution for smaller subhalos. We use two additional samples to probe the subhalo distribution given two different ways of selecting subhalos. In the first, galaxies and satellite galaxies are associated with halos and subhalos, and selection is based on the r -band galaxy luminosities assigned in such a way that the observed luminosity function of galaxies, their clustering, and galaxy-mass correlations are well reproduced (see § 2 and Tasitsiomi et al. 2004, for details). The selection criteria of the primary galaxies and satellites mimic those applied to the SDSS samples. This sample is analogous to Test Sample 3 (see § 2), except that our sample is taken at $z = 0$. Conroy, Wechsler, & Kravtsov (2005b) present a very promising modification to the luminosity assignment scheme discussed which, coupled with high-resolution dissipationless simulations, reproduces the small-scale galaxy clustering and its luminosity dependence observed in SDSS remarkably well. This scheme assigns r -band galaxy luminosities for subhalos not on the V_{\max} at $z = 0$ but using the V_{\max} at the epoch of accretion for the subhalo. Given that the baryonic components of subhalos should be more resistant to the physical processes that evolve the properties of subhalos as they fall into their parent halo, this sample should better reflect the distribution of satellite galaxies. Finally, we use the same primaries as for the subhalo sample, but the satellite sample is now constructed by randomly sampling DM particles surrounding primaries.

Figure 12 shows the interloper-corrected profile for our volume-limited SDSS sample along with the profiles for the true satellites distribution for satellites assigned luminosities by V_{\max} at $z = 0$ and V_{\max} at accretion and the sample of dark matter particles around halos with V_{\max} values in the range $200 - 300 \text{ km s}^{-1}$. The normalization of the dark matter particle profile is set arbitrarily in the

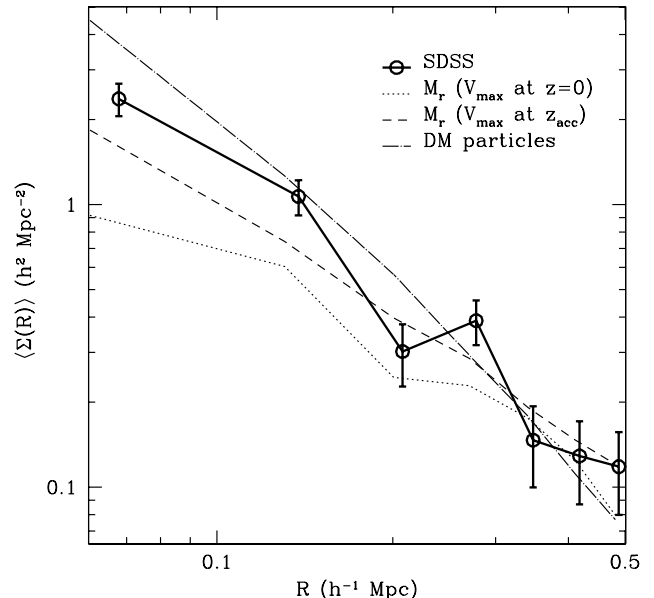


FIG. 12.— Comparison of the projected number density of satellites in the volume-limited SDSS sample (*open circles with error bars connected by the solid line*) and in the three mock satellite simulation-derived samples (see text for details). The *dot-dashed* line represents dark matter distribution around primary halos in simulations, while *dotted* and *dashed* lines show satellite profiles using two different ways of assigning luminosities to subhalos (see text).

plot. The figure shows that the shape of the profiles for all three simulation-derived samples is similar to that of the SDSS sample. The distribution for satellites assigned luminosities by V_{\max} at $z = 0$, however, is shallower than the observed distribution. The distribution for satellites assigned luminosities by V_{\max} at accretion also appears somewhat shallower, but less so than for the other luminosity assignment. The dark matter particles, on the other hand, have a somewhat steeper radial profile than the observed satellites.

Figure 13 compares the best fit slopes for the full range of radii for the different simulation-derived samples discussed above with the corresponding best fit slope for the radial profile of the SDSS satellites. We present radial distributions of subhalos and dark matter particles for the host halos in three ranges of V_{\max} to illustrate the dependence of the satellite distribution of the parent system mass. For the V_{\max} -selected subhalo catalog for primary systems with $V_{\max} = 200 - 300 \text{ km s}^{-1}$, the slope and normalization of the distribution are in reasonable agreement with the data at the 2σ level. The slope is somewhat shallower ($\alpha \approx -1.3 - 1.4$) than observed, but overlap with the latter within the uncertainties. The slope of the corresponding catalog in which satellites are selected from DM particles, exhibit a somewhat steeper slope ($\alpha \approx -1.8$) than observed for the SDSS galaxies, although the difference is not statistically significant. Note that the normalization, A , for this sample is not meaningful, while it is meaningful for the subhalo sample. For primary systems with larger V_{\max} ranges, the subhalo radial distribution becomes progressively shallower than the

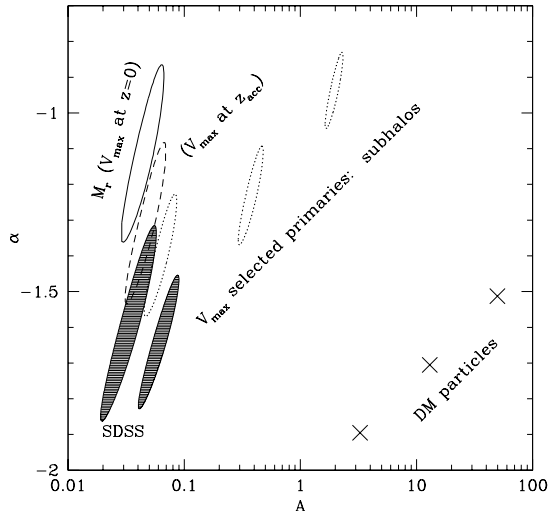


FIG. 13.— The 95.4% confidence intervals for the best-fit power-laws of the interloper subtracted data and for the true satellite distributions of several samples drawn from the simulations. The two filled contours represent the volume-limited sample (on the left) and the flux-limited sample (on the right). The *solid* and *dashed* contours show satellite samples using two different luminosity assignment schemes, as discussed in the text. Samples are drawn from V_{\max} selected primary samples for subhalos with $V_{\max} > 100 \text{ km s}^{-1}$ (dotted contour lines) and for DM particles (crosses), with the V_{\max} ranges of 200-300, 300-400, and 400-600 km s^{-1} showing increasingly shallower slopes and larger amplitudes. The normalization, A , for samples of DM particles is not meaningful, as the samples are drawn from arbitrary fractions of DM particles around host halos.

data because the fixed projected radial range used probes different radii with respect to the halo virial radii. Most of the primaries in our sample should correspond to halos with $V_{\max} < 300 \text{ km s}^{-1}$, so it is not surprising that the data matches the subhalo distribution for primaries with $V_{\max} = 200 - 300 \text{ km s}^{-1}$ the best. For primaries of this size, the virial radius is expected to significantly smaller than $500 h^{-1} \text{ kpc}$, the maximum projected radius measured. Simulations, however, show bound subhalos at several times the virial radii of the host halos.

Figure 13 also compares the best fit slopes for the SDSS to satellite samples with different luminosity assignments. Both assignments are in agreement with the best fit slope of the SDSS volume-limited sample at the 2σ level. Assigning luminosities based on a subhalo mass at accretion, however, results in a steeper slope than assigning luminosities based on a subhalo mass at $z = 0$ and is more consistent with the data.

As previously discussed, the slopes of satellite surface density profiles around SDSS galaxies are in between those measured for subhalos and those for dark matter distributions in simulations of the concordance cosmology, and the measured slopes are closer to those measured for dark matter distribution. In addition, the bias in the interloper subtraction methods suggest that the true satellite distribution is somewhat steeper than our best fit value and even more compatible with the dark matter distribution. Our results are in qualitative agreement with the recent observational studies on the radial distribution of galaxies in groups and clusters (e.g.,

TABLE 7
ESTIMATED POWER-LAW SLOPES FOR DIFFERENT SAMPLES OF TRUE SATELLITES

Primary+satellite sample	$R_{\min} < R < 0.5$	$0.1 < R < 0.5$
SDSS (volume)	-1.58 ± 0.11	-1.77 ± 0.23
SDSS (flux)	-1.64 ± 0.07	-1.72 ± 0.17
M_r (V_{\max} at $z=0$)	-1.12 ± 0.10	-1.36 ± 0.18
M_r (V_{\max} at z_{acc})	-1.31 ± 0.09	-1.38 ± 0.17
$V_{\max} = 200\text{-}300$ (DM)	-1.895 ± 0.010	-2.111 ± 0.020
$V_{\max} = 200\text{-}300$ (subs)	-1.40 ± 0.07	-1.65 ± 0.13
$V_{\max} = 300\text{-}400$ (DM)	-1.705 ± 0.009	-1.864 ± 0.018
$V_{\max} = 300\text{-}400$ (subs)	-1.23 ± 0.06	-1.65 ± 0.11
$V_{\max} = 400\text{-}600$ (DM)	-1.513 ± 0.008	-1.674 ± 0.015
$V_{\max} = 400\text{-}600$ (subs)	-0.94 ± 0.04	-1.26 ± 0.07

Note – Samples using isolated halos chosen by V_{\max} and subhalos assigned a r -band luminosity use binning of $70h^{-1} \text{ kpc}$, with first bin starting at $R_{\min} = 25.6h^{-1} \text{ kpc}$. Subhalos in these samples are selected to have circular velocities $V_{\max} \geq 100 \text{ km s}^{-1}$. Data samples use binning previously described in the text.

Lin et al. 2004; Hansen et al. 2005; Collister & Lahav 2005; Yang et al. 2005; Coil et al. 2006), which find concentrations of galaxy radial profiles somewhat lower than the concentrations expected for the matter distribution of their parent halos. However, here we seem to find that the difference between the DM distribution and the satellite distribution is not as large in galaxy-sized systems compared to groups and clusters.

Several previous studies which considered satellite distribution in *cluster-sized* halos showed that subhalos appear to have more extended and shallower radial distributions compared to that of dark matter (Ghigna et al. 1998; Colín et al. 1999; Ghigna et al. 2000; Springel et al. 2001; De Lucia et al. 2004; Diemand et al. 2004; Gao et al. 2004; Nagai & Kravtsov 2005). Tidal evolution and merging modify the subhalo profile, especially within inner $\sim 50\%$ of the virial radius, primarily because they modify properties of subhalos, such as its bound mass or circular velocity (Nagai & Kravtsov 2005). For galaxy-sized systems in our simulations, then, we would thus expect subhalo profile to be significantly flattened at $R \lesssim 100h^{-1} \text{ kpc}$. Table 7 presents the best-fit slopes for the full range of radii and for the fits restricted to radii between 0.1 and $0.5h^{-1} \text{ Mpc}$ for all the data and simulation samples discussed. The table shows that the best-fit power-laws for bins of $R > 100h^{-1} \text{ kpc}$ are steeper than for those including smaller projected radii. This is generically true, but in particular subhalo distributions seem to steepen more than the DM distributions, suggesting that subhalo distributions are flattened within $\sim 50\%$ of the virial radius as in cluster-sized halos. For example, for subhalos assigned luminosities at $z = 0$, the slope for the restricted set of radii is $-1.36 \pm 0.18 - \approx 0.2$ steeper than the fit using all data points – and the slope steepens further if we constrain the fit to even larger radii, where the best fit slope values of DM and subhalo distributions agree within error bars (note, however, that at these radii the fit errors become larger). On the other hand, the slope for subhalos assigned luminosities at the epoch of accretion and the observational results steepen less, as would be expected given that the baryonic components

of subhalos should be more resistant tidal evolution and merging. We attribute some of the differences in slopes and shallower slopes for our simulation satellite samples to tidal evolution effects, and to the differences in object selection in simulation and SDSS samples (Nagai & Kravtsov 2005). A better understanding of the differences between selection criteria is necessary for more stringent tests of the theoretical predictions.

5. DISCUSSION AND CONCLUSIONS

Modern large galaxy redshift surveys allow one to study the distribution of satellites around galaxies and clusters with unprecedented statistical power, while controlling biases and completeness in a systematic way. In addition, redshift information can be used to select galaxies from relatively non-crowded environments and to account for interloper contamination in a rigorous way. Cosmological simulations are also sufficiently mature and allow systematic tests of the interloper subtraction algorithms. Galaxy and satellite samples, for instance, can be constructed to mimic observational selection criteria. Examples of studies using such surveys are constraints on the DM halos of galaxies from satellite kinematics (McKay et al. 2002; Prada et al. 2003; Brainerd 2005b) and the anisotropy of the distribution of satellite galaxies (Sales & Lambas 2004; Brainerd 2005a).

In this work, we use the SDSS spectroscopic survey to estimate the projected radial distribution of satellites around isolated primaries. We use areas of the survey which are at least 90% complete and check for the effects of incompleteness by comparing the surface density profile and conclude that our results are not affected by the (small) incompleteness of the sample. We construct samples of primary and satellite galaxies with isolation criteria similar to those used by Prada et al. (2003). We use high-resolution cosmological simulations of the concordance Λ CDM cosmology to develop and carefully test new methods of correcting for interloper contamination. Our main results and conclusions can be summarized as follows.

1. Using mock galaxy catalogs derived from high-resolution cosmological simulations, we show that interlopers can significantly bias the shape of the projected surface density profile of faint satellites around bright galaxies, making it shallower (biasing the power-law slope α of the radial profile, $\Sigma(R) \propto R^\alpha$, by $\Delta\alpha_{\text{bias}} \gtrsim 0.5$). We also show that the most straightforward methods do not correct interloper contamination properly. For example, the random points method, which assumes uniform distribution of interlopers in space, underestimates the fraction of interlopers in the satellite sample by oversampling voids compared to clustered areas where most galaxies in the sample reside.
2. We develop two new methods to account for the interloper contamination: the clustered random points method and the nearby points method, variants of the random points method, designed to sample environments similar to those of the clustered galaxies in the observed samples. Tests on the mock samples show that the methods perform consistently well, reducing the interloper bias in the

best-fit power-law slopes of the satellite profiles to only $\Delta\alpha_{\text{bias}} \approx 0.1$ for the nearby points method.

3. We apply these methods in our analyses of the volume- and flux-limited SDSS spectroscopic samples. The best fit power-law slope for the volume-limited SDSS satellite sample, after interloper contamination correction, is -1.58 ± 0.11 in the range of projected separations of $32.9 < R < 500h^{-1}$ kpc. Note that we estimated a systematic bias in the derived slope of $\Delta\alpha_{\text{bias}} \approx 0.1$ for nearby points interloper subtraction method, which implies that the true slope of the SDSS satellites may be $\alpha = \alpha_{\text{raw}} - \Delta\alpha_{\text{bias}} \approx -1.7$. We find similar values of the best fit slopes for the flux-limited samples, and for samples of primary galaxies in different absolute magnitude ranges. We thus do not find evidence for the dependence of the shape of satellite radial distribution on the luminosity of their host galaxy.
4. Comparison of the observed radial distribution of the SDSS satellites to the distribution of subhalos and dark matter around galactic halos in dissipationless Λ CDM simulations shows that the slope of the SDSS satellite radial profile is in between those measured for subhalos and for dark matter (closer to dark matter). Subhalos thus appear to have more extended and shallower radial distributions than the observed satellites. The dark matter distribution is somewhat steeper than the observed satellite profiles, but the difference is not statistically significant.

Recently, van den Bosch et al. (2005) and Sales & Lambas (2005) studied the projected radial distribution of satellite galaxies around isolated galaxies using the Two Degree Field Galaxy Redshift Survey (2dFGRS). van den Bosch et al. (2005) used mock galaxy redshift samples derived from large cosmological simulations to develop an iterative method of interloper rejection for the 2dFGRS and found that the data is generally consistent with the dark matter profile at large projected radii, but concluded that incompleteness of close pairs in the survey prevent strong constraints. Sales & Lambas (2005) used isolation criteria for the primary galaxies, enforcing that any neighbor within a region of $700 h^{-1}$ kpc and $\Delta V = 1000 \text{ km s}^{-1}$ must be at least 1 magnitude fainter. Satellites were assumed to be any object within projected separation of 500 kpc and $\Delta V = 500 \text{ km s}^{-1}$ that is at least 2 magnitudes fainter than the host galaxy. Sales & Lambas (2005) estimated the effect of close-pair incompleteness by deriving a control sample of projected satellites with velocity difference of $2000 < \Delta V < 10,000 \text{ km s}^{-1}$. At $R \gtrsim 20 h^{-1}$ kpc, where the number density profile of the control sample is flat, the satellite samples were considered complete. For the total sample, Sales & Lambas (2005) quoted the best-fit power-law of slope $\alpha = -0.96 \pm 0.03$. This value, however, was derived without applying correction for interloper contamination. Note that we derive significantly steeper profiles of satellites compared to those of Sales & Lambas (2005), which we attribute to the rigorous correction for interlopers and to possible fiber-collision bias in the 2dFGRS.

The results presented in this study provide interesting hints of the possible differences between observed satellite distributions and the expected distribution of subhalos in their parent halos. However, the statistical errors are still rather large. Significant improvements in the statistics are needed to address this question further. Larger statistics would also allow us to go beyond the average profiles and study the distribution of satellites as a function of satellite (e.g., luminosity and color) and host galaxy properties.

We would like to thank Risa Wechsler for her help with the luminosity assignment for the halo catalogs and Charlie Conroy for a careful reading of the manuscript and useful comments. This research was carried out at the University of Chicago, Kavli Institute for Cosmological Physics and was supported (in part) by grant NSF PHY-0114422. KICP is an NSF Physics Frontier Center. JC and AVK were supported by the National Science Foundation (NSF) under grants No. AST-0206216, AST-0239759 and AST-0507666, and by NASA through grant NAG5-13274. Cosmological simulations used in this analysis were performed on the IBM RS/6000 SP3

system (*seaborg*) at the National Energy Research Scientific Computing Center (NERSC). This work has made use of the NASA Astrophysics Data System.

Funding for the creation and distribution of the SDSS Archive has been provided by the Alfred P. Sloan Foundation, the Participating Institutions, the National Aeronautics and Space Administration, the National Science Foundation, the U.S. Department of Energy, the Japanese Monbukagakusho, and the Max Planck Society. The SDSS Web site is <http://www.sdss.org/>.

The SDSS is managed by the Astrophysical Research Consortium (ARC) for the Participating Institutions. The Participating Institutions are The University of Chicago, Fermilab, the Institute for Advanced Study, the Japan Participation Group, The Johns Hopkins University, the Korean Scientist Group, Los Alamos National Laboratory, the Max-Planck-Institute for Astronomy (MPIA), the Max-Planck-Institute for Astrophysics (MPA), New Mexico State University, University of Pittsburgh, University of Portsmouth, Princeton University, the United States Naval Observatory, and the University of Washington.

REFERENCES

- Abazajian, K., et al. 2005, *AJ*, 129, 1755
 Adelman-McCarthy, J. K., et al. 2006, *ApJS*, 162, 38
 Blanton, M. R., Brinkmann, J., Csabai, I., Doi, M., Eisenstein, D., Fukugita, M., Gunn, J. E., Hogg, D. W., & Schlegel, D. J. 2003a, *AJ*, 125, 2348
 Blanton, M. R., Lin, H., Lupton, R. H., Maley, F. M., Young, N., Zehavi, I., & Loveday, J. 2003b, *AJ*, 125, 2276
 Blanton, M. R., Schlegel, D. J., Strauss, M. A., Brinkmann, J., Finkbeiner, D., Fukugita, M., Gunn, J. E., Hogg, D. W., Ivezić, Ž., Knapp, G. R., Lupton, R. H., Munn, J. A., Schneider, D. P., Tegmark, M., & Zehavi, I. 2005, *AJ*, 129, 2562
 Blanton, M. R., et al. 2003c, *ApJ*, 592, 819
 Brainerd, T. G. 2005a, *ApJ*, 628, L101
 —. 2005b, *ApJ*, submitted (astro-ph/0409381)
 Coil, A. L., Gerke, B. F., Newman, J. A., Ma, C.-P., Yan, R., Cooper, M. C., Davis, M., Faber, S. M., Guhathakurta, P., & Koo, D. C. 2006, *ApJ*, 638, 668
 Colín, P., Klypin, A. A., Kravtsov, A. V., & Khokhlov, A. M. 1999, *ApJ*, 523, 32
 Collister, A. A., & Lahav, O. 2005, *MNRAS*, 361, 415
 Conroy, C., Newman, J. A., Davis, M., Coil, A. L., Yan, R., Cooper, M. C., Gerke, B. F., Faber, S. M., & Koo, D. C. 2005a, *ApJ*, 635, 982
 Conroy, C., Wechsler, R. H., & Kravtsov, A. V. 2005b, *ApJ* submitted (astro-ph/0512234)
 De Lucia, G., Kauffmann, G., Springel, V., White, S. D. M., Lanzoni, B., Stoehr, F., Tormen, G., & Yoshida, N. 2004, *MNRAS*, 348, 333
 Diemand, J., Madau, P., & Moore, B. 2005, *MNRAS*, 364, 367
 Diemand, J., Moore, B., & Stadel, J. 2004, *MNRAS*, 352, 535
 Fukugita, M., Ichikawa, T., Gunn, J. E., Doi, M., Shimasaku, K., & Schneider, D. P. 1996, *AJ*, 111, 1748
 Gao, L., White, S. D. M., Jenkins, A., Stoehr, F., & Springel, V. 2004, *MNRAS*, 355, 819
 Ghigna, S., Moore, B., Governato, F., Lake, G., Quinn, T., & Stadel, J. 1998, *MNRAS*, 300, 146
 —. 2000, *ApJ*, 544, 616
 Gunn, J. E., et al. 1998, *AJ*, 116, 3040
 —. 2006, *AJ*, submitted
 Hansen, S. M., McKay, T. A., Wechsler, R. H., Annis, J., Sheldon, E. S., & Kimball, A. 2005, *ApJ*, 633, 122
 Hogg, D. W., Finkbeiner, D. P., Schlegel, D. J., & Gunn, J. E. 2001, *AJ*, 122, 2129
 Ivezić, Ž., et al. 2004, *Astronomische Nachrichten*, 325, 583
 Klypin, A., Gottlöber, S., Kravtsov, A. V., & Khokhlov, A. M. 1999a, *ApJ*, 516, 530
 Klypin, A., Kravtsov, A. V., Valenzuela, O., & Prada, F. 1999b, *ApJ*, 522, 82
 Kravtsov, A. V. 1999, Ph.D. Thesis
 Kravtsov, A. V., Berlind, A. A., Wechsler, R. H., Klypin, A. A., Gottlöber, S., Allgood, B., & Primack, J. R. 2004a, *ApJ*, 609, 35
 Kravtsov, A. V., Gnedin, O. Y., & Klypin, A. A. 2004b, *ApJ*, 609, 482
 Kravtsov, A. V., Klypin, A. A., & Khokhlov, A. M. 1997, *ApJS*, 111, 73
 Lake, G., & Tremaine, S. 1980, *ApJ*, 238, L13
 Lin, Y.-T., Mohr, J. J., & Stanford, S. A. 2004, *ApJ*, 610, 745
 Lorrimer, S. J., Frenk, C. S., Smith, R. M., White, S. D. M., & Zaritsky, D. 1994, *MNRAS*, 269, 696
 Madore, B. F., Freedman, W. L., & Bothun, G. D. 2004, *ApJ*, 607, 810
 McKay, T. A., Sheldon, E. S., Johnston, D., Grebel, E. K., Prada, F., Rix, H., Bahcall, N. A., Brinkmann, J., Csabai, I., Fukugita, M., Lamb, D. Q., & York, D. G. 2002, *ApJ*, 571, L85
 Moore, B., Ghigna, S., Governato, F., Lake, G., Quinn, T., Stadel, J., & Tozzi, P. 1999, *ApJ*, 524, L19
 Nagai, D., & Kravtsov, A. V. 2005, *ApJ*, 618, 557
 Navarro, J. F., Frenk, C. S., & White, S. D. M. 1997, *ApJ*, 490, 493
 Phillipps, S., & Shanks, T. 1987, *MNRAS*, 229, 621
 Pier, J. R., Munn, J. A., Hindsley, R. B., Hennessy, G. S., Kent, S. M., Lupton, R. H., & Ivezić, Ž. 2003, *AJ*, 125, 1559
 Prada, F., Vitvitska, M., Klypin, A., Holtzman, J. A., Schlegel, D. J., Grebel, E. K., Rix, H.-W., Brinkmann, J., McKay, T. A., & Csabai, I. 2003, *ApJ*, 598, 260
 Sales, L., & Lambas, D. G. 2004, *MNRAS*, 348, 1236
 —. 2005, *MNRAS*, 356, 1045
 Smith, J. A., et al. 2002, *AJ*, 123, 2121
 Smith, R. M., Martínez, V. J., & Graham, M. J. 2004, *ApJ*, 617, 1017
 Springel, V., White, S. D. M., Tormen, G., & Kauffmann, G. 2001, *MNRAS*, 328, 726
 Stoughton, C., et al. 2002, *AJ*, 123, 485
 Strauss, M. A., et al. 2002, *AJ*, 124, 1810
 Tasitsiomi, A., Kravtsov, A. V., Gottlöber, S., & Klypin, A. A. 2004, *ApJ*, 607, 125
 Taylor, J. E., Silk, J., & Babul, A. 2004, in *IAU Symposium*, 91
 Tegmark, M., et al. 2004, *ApJ*, 606, 702
 Vader, J. P., & Sandage, A. 1991, *ApJ*, 379, L1
 van den Bosch, F. C., Norberg, P., Mo, H. J., & Yang, X. 2004, *MNRAS*, 352, 1302
 van den Bosch, F. C., Yang, X., Mo, H. J., & Norberg, P. 2005, *MNRAS*, 356, 1233

Willman, B., Governato, F., Dalcanton, J. J., Reed, D., & Quinn, T. 2004, MNRAS, 353, 639
Yang, X., Mo, H. J., van den Bosch, F. C., Weinmann, S. M., Li, C., & Jing, Y. P. 2005, MNRAS, 362, 711
York, D. G., et al. 2000, AJ, 120, 1579
Zaritsky, D., Smith, R., Frenk, C., & White, S. D. M. 1997, ApJ, 478, 39

Zaritsky, D., & White, S. D. M. 1994, ApJ, 435, 599
Zehavi, I., Weinberg, D. H., Zheng, Z., et al. 2004, ApJ, 608, 16